



Single-layer MoS₂ with adjacent Mo sites for efficient electrocatalytic nitrogen fixation via spin-delocalized electrons effect

Guangming Zhan^{a,b,1}, Fengjiao Quan^{b,1}, Yancai Yao^{a,*}, Shengxi Zhao^b, Xiufan Liu^b, Huayu Gu^b, Yi Huang^b, Xiao Liu^b, Falong Jia^b, Lizhi Zhang^{a,b,**}

^a School of Environmental Science and Engineering, Shanghai Jiao Tong University, Shanghai 200240, PR China

^b Key Laboratory of Pesticide & Chemical Biology of Ministry of Education, Institute of Environmental & Applied Chemistry, College of Chemistry, Central China Normal University, Wuhan 430079, PR China

ARTICLE INFO

Keywords:

Electrocatalytic nitrogen fixation
Single-layer MoS₂
Adjacent Mo sites
Spin-delocalized electrons

ABSTRACT

Electrocatalytic nitrogen fixation is crucial for sustainable NH₃ production, however it still suffers from sluggish kinetics. Here, we report that single-layer MoS₂ with adjacent Mo sites (A-Mo-MoS₂) prepared by precisely controlling the oriented topological conversion could exhibit an exceptional NH₃ yield rate of 48.8 μg h⁻¹ mg⁻¹ and Faradic efficiency (FE) of 27.3 % at -0.20 V vs. RHE, far beyond MoS₂ with isolated sulfur vacancies (I-SV-MoS₂) with a 18.8 μg h⁻¹ mg⁻¹ rate and 8.4 % FE. Theoretical analysis reveal that A-Mo-MoS₂ could induce their unpaired spin-polarized electrons to share along the outermost Mo edge, thereby forming a grand spin-delocalized electrons reservoir. Compared to limited spin-localized electrons on I-SV-MoS₂, these spin-delocalized electrons could significantly facilitate nitrogen activation and switched the rate-determining step from energy-demanding *N₂ hydrogenation to surmountable *HNNH hydrogenation. Our work offers a new strategy to promote nitrogen fixation by spin-delocalized electrons effect.

1. Introduction

Renewable energy driven electrocatalytic nitrogen (N₂) fixation to produce ammonia (NH₃) is regarded as one of the most important chemical transformations [1–3]. Despite much progress in sustainable electrocatalytic N₂ fixation, challenges to achieve low overpotential and high Faradic efficiency (FE) towards NH₃ are still imperative to be addressed [4,5]. In essence, these challenges emanate from the fact that the electrocatalyst's electrons could not activate N₂ effectively, owing to its formidable N≡N triple bond (941 kJ mol⁻¹) and non-polar nature [6–8]. Generally, noble metal electrocatalysts, such as Ru/Rh-based nanomaterials, exhibit remarkable N₂ fixation ability [9,10]. However, the high cost and scarcity greatly limit their practical application. Thus, the development of efficient and inexpensive electrocatalysts is of great significance for realizing the sustainable N₂-to-NH₃ scenario [11–13].

Single-layer molybdenum disulfide (MoS₂), featured with nitrogenase-like configuration, unique electronic structure and reactive edge sites, has triggered considerable interest as the most promising

non-noble-metal material for electrocatalytic N₂ fixation [14–17]. The partially occupied d-orbital of Mo atom can donate electrons to the empty π-antibonding orbital of N₂ and simultaneously accept the unpaired electrons from the σ-orbital of N₂, thus promoting the activation of stubborn N≡N [18,19]. Despite possessing this superiority, the electrocatalytic N₂ fixation performance of single-layer MoS₂ is still depressed with a NH₃ yield rate and FE usually less than 20 μg h⁻¹ mg⁻¹ and 8 %, respectively [20–22]. Recently, researchers demonstrated that the introduction of sulfur vacancies (SVs) could improve the electrocatalytic N₂ fixation efficiency of single-layer MoS₂, highly depending on the spin-polarized electrons of SVs [23,24]. Nevertheless, these finite spin-polarized electrons on SVs are quickly exhausted and therefore unaffordable for activating the energy-demanding N≡N effectively. Meanwhile, these spin-polarized electrons are confined to form spin-localized electrons on isolated SV, disfavoring the electron's donation among different SVs, consequently resulting in limited N₂ activation because of insufficient electrons [25].

Distinct from spin-localized electrons, spin-delocalized electrons are

* Corresponding author.

** Corresponding author at: School of Environmental Science and Engineering, Shanghai Jiao Tong University, Shanghai 200240, PR China.

E-mail addresses: yyancai@sjtu.edu.cn (Y. Yao), zhanglz@mail.ccnu.edu.cn, zhanglizhi@sjtu.edu.cn (L. Zhang).

¹ These authors contributed equally to this work.

not confined to specific adsorbed sites, forming a shared spin-delocalized electrons reservoir [26,27]. As a result, spin-delocalized electrons would favor the N_2 activation, rendering the cleavage of stubborn $N\equiv N$ with a surmountable barrier potentially. Theoretically, terminated adjacent Mo sites on single-layer MoS_2 with plentiful unpaired electrons can induce the spin-polarized electrons to share among adjacent Mo atoms, forming a grand spin-delocalized electrons field. Meanwhile, these adjacent Mo sites can build up an effective channel for the delivery of spin-delocalized electrons from the adjacent Mo atoms to the adsorbed N_2 and thus destroying the $N\equiv N$ bond efficiently [28]. However, electrocatalytic N_2 fixation performance of single layer MoS_2 with adjacent Mo sites has not been investigated previously, because MoS_2 with adjacent Mo sites is less thermodynamically instable than MoS_2 with a stable S-termination, and usually prepared with tedious synthetic processes, harsh experimental conditions and complicated/expensive equipment [29–32]. Thus, the development of a simple and mild approach for the synthesis of single layer MoS_2 with adjacent Mo sites is highly desired.

Herein, we develop an oriented topological structural conversion strategy to successfully fabricate adjacent Mo sites on the outermost edge of single-layer MoS_2 under mild conditions. The resultant single-layer MoS_2 with adjacent Mo sites is comprehensively characterized and compared with single-layer MoS_2 with isolated sulfur vacancies on electrocatalytic N_2 fixation, aiming to elucidate the contribution of spin-delocalized electrons from the adjacent Mo atoms to N_2 activation for the first time.

2. Materials and methods

2.1. Materials synthesis

2.1.1. Preparation of flower-like bulk MoS_2 nanosheets

Typically, $Na_2MoO_4 \cdot 2H_2O$ (7 mmol) and thiourea (24 mmol) were first solved in distilled water (50 mL) under sonication at room temperature for 30 min to obtain a homogeneous solution. Then, the mixture solution was transferred into an 80 mL Teflon-lined autoclave and maintained 200 °C for 24 h under autogenous pressure, and then cooled to room temperature. The product was collected by centrifugation at 10,000 rpm for 10 min, washed with 0.1 M HCl and ethanol for at least 4 times, and finally dried at 50 °C under vacuum. The obtained sample was flower-like bulk MoS_2 nanosheets with stable S termination.

2.1.2. Preparation of S- MoS_2 and I-SV- MoS_2

Single-layer S- MoS_2 was prepared by exfoliating original bulk MoS_2 nanosheets using the organolithium chemistry method. Briefly, 0.2 g of bulk MoS_2 nanosheets was immersed in 8 mL of n-butyllithium under Ar atmosphere for 72 h at 100 °C. The suspension was then washed with hexane for several times to remove the excess of n-butyllithium. The collected nanosheets with lithium intercalation were re-dispersed with a concentration of 1 mg/mL and sonicated by an ultrasonic cell disrupter system for 12 h to obtain exfoliated nanosheets. After centrifuging the resultant suspension at 5000 rpm for 10 min, the supernatants were collected and removed the unsuccessfully exfoliated nanosheets. The collected supernatants were again centrifuged at 12,000 rpm for 10 min to obtain single-layer S- MoS_2 .

Single-layer I-SV- MoS_2 was obtained by thermally reduction of single-layer S- MoS_2 under 5 % H_2 -Ar mixture gas (60 mL min⁻¹) at 500 °C for 2 h.

2.1.3. Preparation of A- Mo - MoS_2

0.2 g of as-prepared flower-like bulk MoS_2 nanosheets was slowly added into 50 mL 0.1 M NaBH₄ and 0.05 M $Na_2MoO_4 \cdot 2H_2O$ mixed solution with vigorous stirring for 30 min. The mixture was transferred into an 80 mL Teflon-lined autoclave and maintained at 200 °C for 24 h. Under mild hydrothermal condition, bulk MoS_2 nanosheet with S-Mo-S atomic structure was converted to S-Mo-S-Mo structure by precisely

controlling the oriented topological structural conversion driven by high Mo(VI) ions guiding. Then, the produced bulk A-Mo- MoS_2 was collected by centrifugation at 10,000 rpm for 10 min, washed with 0.1 M HCl and ethanol for several times, and finally dried at 50 °C under vacuum. Finally, organolithium chemistry was used to exfoliate bulk A-Mo- MoS_2 nanosheets to their single-layer counterpart.

2.2. Catalysts characterization

The powder XRD patterns were recorded by a Bruker D8 Advance diffractometer with monochromatized Cu-K α ($\lambda = 0.15418$ nm) radiation. The electron paramagnetic resonance (EPR) spectra were collected at room temperature using a Bruker RPE Elexsys E500 spectrometer equipped with a SHQ with X band frequency in a continuous wave (around 9.8 GHz) cavity. ~ 10 mg of MoS_2 powder was loaded in a quartz tube. Spectra were recorded with a modulation amplitude of 3510 G, a modulation frequency of 100 kHz and a microwave power of about 20 mW. Raman spectra were collected at room temperature on a Renishaw Invia Plus instrument using a semiconductor laser as an illumination source (633 nm). The X-ray photoelectron spectroscopy (XPS) measurements were performed with Perkin-Elmer PHI 5000 C and all binding energies were calibrated by using the contaminant carbon ($C_{1s} = 284.6$ eV) as a reference. Transmission electron microscope (TEM) images were obtained using a HRTEM JEOL 2200 FS microscope. The imaging parameters were adjusted on a different region of the sample prior taking any high-resolution images in order to minimize the sample exposure to the electron beam. High angle annular dark field scanning transmission electron microscopy (HAADF-STEM) images were obtained by a fifth order aberration-corrected transmission electron microscope JEOL ARM200CF microscope incorporated with Dual-type EDS detector, EDS (JED-2300T, large effective solid angle (≈ 1.2 sr.) X-ray sensing area of a 100 mm² for each. The acceleration voltage of the microscope was set to 80 kV to decrease knock-on damage. Atomic force microscopy (AFM) was carried out by Veeco DI Nano-scope MultiMode V system.

N_2 temperature-programmed desorption (N_2 -TPD) tests were performed in a quartz reactor with a TCD as detector. 0.3 g catalyst was first pre-treated with pure He with a flow rate of 50 mL min⁻¹ at 120 °C for 30 min, then cooled down to room temperature in the same atmosphere and then feed with pure N_2 . The catalyst was then purged with pure He (99.999%) gas with a flow rate of 50 mL min⁻¹ for 30 min to remove the residual N_2 . Then, the N_2 -TPD measurement was performed up to 500 °C at a heating rate of 5 °C min⁻¹ in the pure He atmosphere. The BET surface area was calculated from the linear part of the BET plot ($P/P_0 = 0.10$ – 0.30). The Fourier transform infrared (FT-IR) spectra were acquired by Nicolet iS50FT-IR spectrometer (Thermo, USA) scanning from 4000 to 400 cm⁻¹ at room temperature.

The Mo K-edge X-ray absorption spectra were measured at beamline 1W1B of the Beijing Synchrotron Radiation Facility (BSRF) in fluorescence mode using a Si (111) double crystal monochromator at room temperature. The data analysis of the XANES spectra was carried out using the ATHENA program. Scattering paths were calculated by FEFF6 from optimized MoS_2 crystal structure. The fitting range of Mo K-edge was $\Delta k = 2.00$ – 13.01 Å⁻¹ and $\Delta R = 1.10$ – 3.14 Å. Plotted spectra were not phase-corrected and have a k -weight of 3.

2.3. Electrocatalytic N_2 fixation measurements

10 mg of as-prepared MoS_2 and 40 μ L of Nafion solution (4 wt%) were dispersed in 960 μ L isopropanol solution by sonicating for 1 h to form a homogeneous ink. 200 μ L catalyst ink was subsequently loaded onto a glassy carbon plate electrode with an area of 1.0×2.0 cm² and dried by an infrared lamp under ambient condition. The mass density of the catalysts is about 1.0 mg/cm². Thereafter, the N_2 fixation activity tests were conducted on a CHI 660D electrochemical workstation in a standard three-electrode cell, in which the cathode and anode were separated by the Nafion-211 membrane. Before N_2 fixation test, the

Nafion-211 membrane was heated in 5 % H_2O_2 , 0.5 M H_2SO_4 , and ultrapure water at 80 °C for 1 h, respectively. A platinum slice and a saturated calomel electrode (SCE) were used as the counter and reference electrodes, respectively. The potentials in this work were converted to RHE scale by the following equation: $E(\text{vs. RHE}) = E(\text{vs. SCE}) + 0.24 + 0.059 \times \text{pH}$, and the pH of electrolyte was measured using Model PHS-3 C pH meter. For electrochemical N_2 reduction, chronoamperometry tests were carried out at different potentials in N_2 -saturated 0.1 M KCl solution, which was purged with N_2 during the electrolysis. To ensure the tests with N_2 -saturated conditions, the solution was purged with N_2 for 30 min before each measurement. The N_2 fixation products were determined by Ion chromatograms and the Watt and Chrisp methods. We monitored the H_2 formation by gas chromatography using a previously reported method [33].

2.4. Calculations of NH_3 yield rate and FE

NH_3 yield rate was calculated using the following equation:

$$\text{NH}_3 \text{ yield rate} = [\text{NH}_4^+] \times V / (m \times t)$$

FE was calculated according to the following equation:

$$\text{FE} = 3 \times F \times [\text{NH}_4^+] \times V / (17 \times Q)$$

where $[\text{NH}_4^+]$ is the measured NH_4^+ ion concentration; V is the volume of the cathodic reaction electrolyte; t is the potential applied time; m is the loaded mass of catalyst; F is the Faraday constant; and Q is the total charge during tests.

2.5. ^1H nuclear magnetic resonance (NMR) Test

^1H NMR (Agilent 600-MHz) was used to quantitate NH_3 concentration of reaction and maleic acid ($\text{C}_4\text{H}_4\text{O}_4$) with a concentration of 0.4 mg L^{-1} was used as the internal standard. The calibration curve was plotted with the concentration of NH_4^+ vs. the peak area ratio of NH_4^+ and $\text{C}_4\text{H}_4\text{O}_4$. For the NMR studies, the pH of solutions was adjusted to 2 by using concentrated hydrochloric acid aqueous solution and 3 % D_2O was added into the solutions. The NH_3 produced was obtained by calculating the peak area based on the calibration curve.

2.6. Computational details

All Spin-polarized density functional theory (DFT) [34,35] calculations were performed using the VASP code [36]. The generalized gradient approximation (GGA) of Perdew-Burke-Ernzerhof (PBE) was used as exchange-correlation functional [37]. The plane wave pseudo-potential with a kinetic cutoff energy of 450 eV within the PAW method was carried out [38,39]. The van der Waals interactions were described using the empirical correction in Grimme's scheme [40]. The A-Mo-MoS₂ and I-SV-MoS₂ were modeled by a 4×4 supercell with 20 Å thick vacuum-layer in the z direction. A grid of $3 \times 3 \times 1$ Monkhorst-Pack k -points was used to perform integration in the first Brillouin zone.

During the geometrical optimization, all structures were relaxed to an energy convergence of 10^{-5} eV/atom and a force convergence of 0.02 eV/Å. Thermal and zero-point energy (ZPE) corrections were calculated over Γ points. The Gaussian smearing method with an electronic temperature of $k_{\text{B}}T = 0.05$ eV was employed. The calculation of the free energy diagrams was performed by using the concept of computational hydrogen electrode (CHE) [41]. The Gibbs free energy change (ΔG) of every elemental step was determined as follows: $\Delta G = \Delta E + \Delta \text{ZPE} - T\Delta S$, where ΔE is the electronic energy difference directly obtained from DFT calculations, ΔZPE is the change in zero-point energies, T is the temperature ($T = 298.15$ K), and ΔS is the entropy change. The zero-point energies and entropies of the N_2 reduction species were computed from the vibrational frequencies, in which only the adsorbate

vibrational modes were calculated explicitly.

The crystal orbital Hamilton population (COHP) was performed to chemical bonding analysis by the LOBSTER package [42–45].

3. Results and discussion

3.1. Synthesis and characterization of single-layer A-Mo-MoS₂

We synthesized the adjacent Mo sites on the outermost edge of single-layer MoS₂ (A-Mo-MoS₂) through an oriented topological growth strategy along with hydrothermal treatment. Specifically, we first prepared the flower-like bulk MoS₂ nanosheets with stable S termination via a previously reported method (Fig. S1) [46]. With bulk MoS₂ nanosheets as crystal seeds, the bulk A-Mo-MoS₂ was generated by precisely controlling the oriented topological structural conversion from S-Mo-S to S-Mo-S-Mo atomic arrangement, driven by high Mo(VI) ions guiding under mild hydrothermal condition (Fig. 1a). Then, bulk A-Mo-MoS₂ was exfoliated to single-layer A-Mo-MoS₂ by distinguished Li-ion intercalating. For comparison, single-layer MoS₂ with S-termination (S-MoS₂) was prepared by directly exfoliation of original bulk MoS₂ nanosheets, and single-layer MoS₂ with isolated sulfur vacancies (I-SV-MoS₂) was prepared by thermally reduction of S-MoS₂ under 5 % H_2/Ar atmosphere. As expected, the A-Mo-MoS₂, I-SV-MoS₂, and S-MoS₂ samples were all in ultrathin nanosheet morphology with the same crystal phase, as confirmed by X-ray diffraction (XRD) patterns with typical diffraction peaks of MoS₂ (Figs. 1b, c and S2) [47]. As shown in the atomic force microscopy (AFM) images, all the average thicknesses of A-Mo-MoS₂, I-SV-MoS₂, and S-MoS₂ nanosheets were estimated to be 0.68 nm, demonstrating their single atomic layer structure (Figs. 1d, e and S3) [48]. We then sought to identify the atomic structures of A-Mo-MoS₂, I-SV-MoS₂, and S-MoS₂ by the aberration-corrected high-angle annular dark-field scanning transmission electron microscopy (HAADF-STEM) depended on the different Z contrasts of atomic columns. Remarkably, a brighter atomic layer was visible on the outermost edge of A-Mo-MoS₂, indicating the adjacent Mo arrangements for all zigzag orientations (Fig. 1f). Different from the atomic arrangement of A-Mo-MoS₂, the outermost edge of I-SV-MoS₂ and S-MoS₂ were obviously darker atomic layer, ascribable to the orderly terminal S atom (Figs. 1g and S4). Meanwhile, S vacancies were clearly visualized on the base plane of I-SV-MoS₂ as highlighted by the green triangle, confirming the successful formation of S vacancies on the S-MoS₂ surface (Fig. 1h, i).

In the Raman spectra (Fig. 1j), two strong peaks around 385 cm^{-1} and 410 cm^{-1} assigned to in-plane $\text{E}_{2\text{g}}$ vibration and out-of-plane $\text{A}_{1\text{g}}$ vibration were visible for A-Mo-MoS₂, I-SV-MoS₂, and S-MoS₂, indicative of their identical 2H crystalline structure. Strikingly, a characteristic peak at 530 cm^{-1} , belonging to the terminal S-S stretching mode of disulfide anions ($[\text{S}-\text{S}]^{2-}$) configuration [49,50], appeared in I-SV-MoS₂ and S-MoS₂ while not in A-Mo-MoS₂, suggesting their differences in terminal atomic structure. Thereafter, we performed X-ray absorption fine structure (XAFS) to check the locally fine structure of A-Mo-MoS₂, I-SV-MoS₂, and S-MoS₂. The Fourier transform (FT) of the extended XAFS (EXAFS) for Mo K-edge was almost identical for A-Mo-MoS₂, I-SV-MoS₂, and S-MoS₂, indicating the similar Mo coordination and smaller S coordination of A-Mo-MoS₂ compared to I-SV-MoS₂ and S-MoS₂ (Fig. 1k), consistent with the wavelet transform (WT) analysis (Fig. S5). According to the quantitative structural parameters acquired from the fitting of EXAFS, the coordination number of Mo species in A-Mo-MoS₂ was just 4.0 ± 0.2 , far less than theoretically coordination saturated number (6.0), strongly evidencing the outermost adjacent Mo arrangement (Figs. 1k, S6 and Table S1). As for I-SV-MoS₂, the coordination number of Mo-S was 4.5 ± 0.2 , less than that of S-MoS₂ counterpart (4.8 ± 0.2), again validating the existence of SVs in I-SV-MoS₂. The chemical state was determined by the X-ray absorption near-edge structure (XANES) combined with X-ray photoelectron spectroscopy (XPS), which both revealed the positively charged Mo species in A-Mo-MoS₂, I-SV-MoS₂, and S-MoS₂ (Figs. 1l, m and S7). However, the

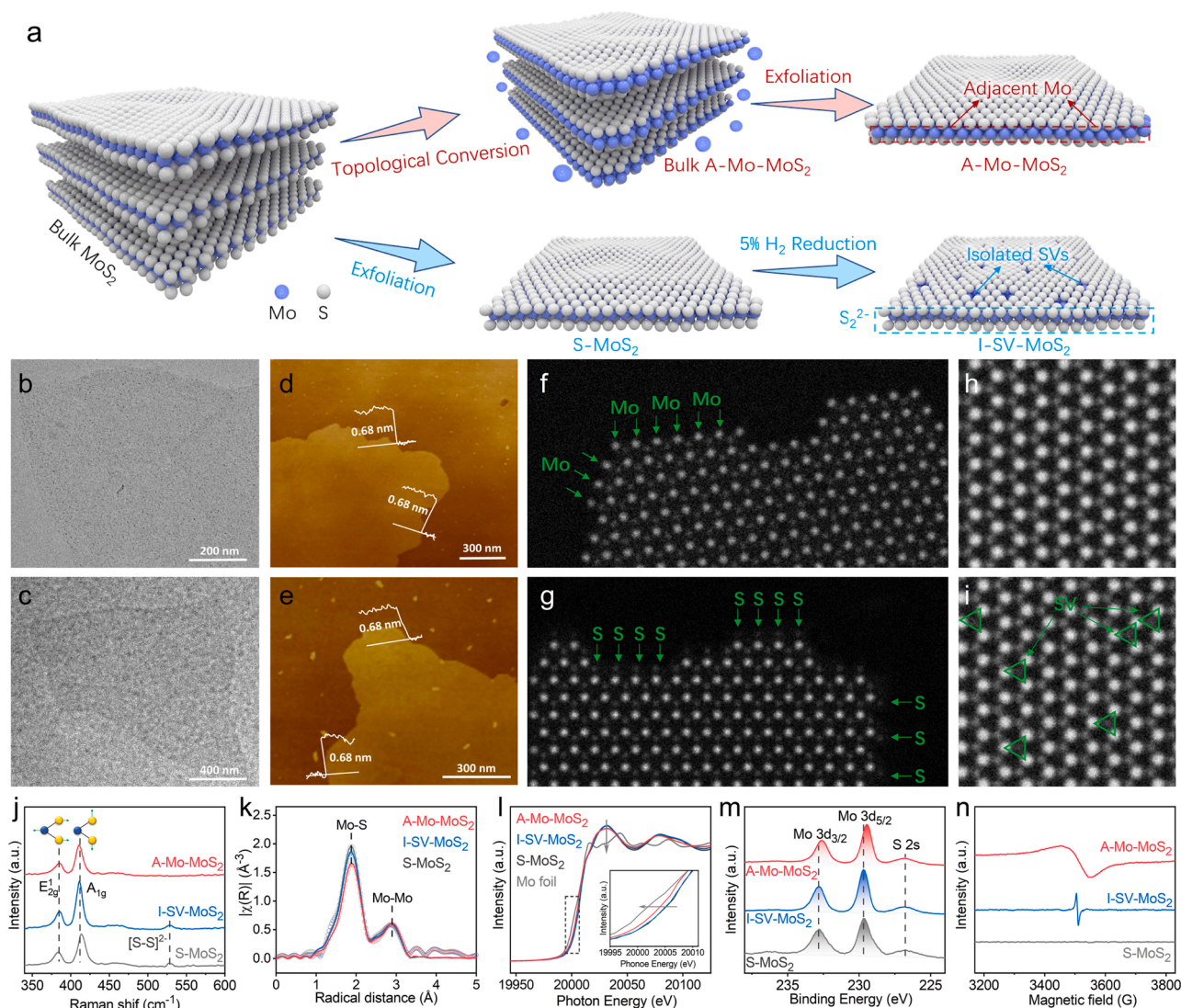


Fig. 1. (a) Illustration showing the synthesis of A-Mo-MoS₂, I-SV-MoS₂, and S-MoS₂. TEM and AFM images with the corresponding height profiles, and basal plane atomic-resolution HAADF-STEM images of A-Mo-MoS₂ (b–e) and I-SV-MoS₂ (f–i). Raman spectra (j), k^3 -weighted Fourier transform EXAFS (k), Mo K-edge XANES (l), high-resolution XPS spectra (m) and ESR spectra (n) of prepared A-Mo-MoS₂, I-SV-MoS₂, and S-MoS₂.

Mo species in A-Mo-MoS₂ exhibited lower valence state arisen from highly unsaturated Mo, as reflected by the shifting of Mo 3d to lower binding energy in comparison with Mo in I-SV-MoS₂ and S-MoS₂.

Then, we checked the electron properties of A-Mo-MoS₂, I-SV-MoS₂, and S-MoS₂ by comparing their electron paramagnetic resonance (EPR) spectra, which is sensitive to the spatial distribution of unpaired spin-polarized electrons. Interestingly, a main peak at ~ 3500 G was both found in A-Mo-MoS₂ and I-SV-MoS₂ (Fig. 1n), rationalized by the outermost adjacent Mo atoms and isolated SVs with unpaired spin-polarized electrons, whereas no EPR signals appeared in the S-MoS₂. It was found that A-Mo-MoS₂ possessed a broader peak at ~ 3500 G than I-SV-MoS₂, which might be originated from magnetic interactions with unpaired spin-polarized electrons of adjacent Mo sites, resulting in the delocalization of unpaired spin-polarized electrons [51–53]. In contrast, the sharp EPR peak of I-SV-MoS₂ reflected the localized spin-polarized electrons on isolated SVs. These results were further confirmed by the appearance of overlapping signal of the localized and delocalized unpaired spin-polarized electrons in the EPR spectrum after introducing SVs in A-Mo-MoS₂ (Fig. S8).

3.2. Electrocatalytic N₂ fixation performance of single-layer A-Mo-MoS₂

We then evaluated the electrocatalytic N₂ fixation activity of A-Mo-MoS₂ and compared it with I-SV-MoS₂ and S-MoS₂ via a standard flow chart (Fig. S9) [22,54]. As shown by the linear sweep voltammetry (LSV), the A-Mo-MoS₂ presented a larger current density enhancement when the Ar-bubbling was changed to N₂-bubbling in 0.1 M KCl solution (Fig. 2a), implying its stronger N₂ fixation activity. The negligible current density variation of S-MoS₂ suggested its extremely poor N₂ fixation ability, as verified by almost no NH₃ detected by Ion chromatogram under the working potential from 0 to -0.40 V vs. reversible hydrogen electrode (RHE) (Figs. S10 and S11). We further investigated the potential-dependent N₂ fixation activity of A-Mo-MoS₂ and I-SV-MoS₂, and found an expected volcano-type relation between the activity and the applied potentials. The highest FE of A-Mo-MoS₂ was up to 27.3 % with an excellent NH₃ yield rate of $48.8 \mu\text{g h}^{-1} \text{mg}^{-1}$, surpassing those of I-SV-MoS₂ with a FE of 8.4 % and NH₃ yield rate of $18.8 \mu\text{g h}^{-1} \text{mg}^{-1}$ at -0.20 V vs. RHE (Figs. 2b, S12–14). Strikingly, this impressive performance of A-Mo-MoS₂ outperformed those of most reported MoS₂-based and other non-noble metal electrocatalysts (Table S2) [15–17, 55–65]. Except for H₂, no other common byproduct N₂H₄ was detected

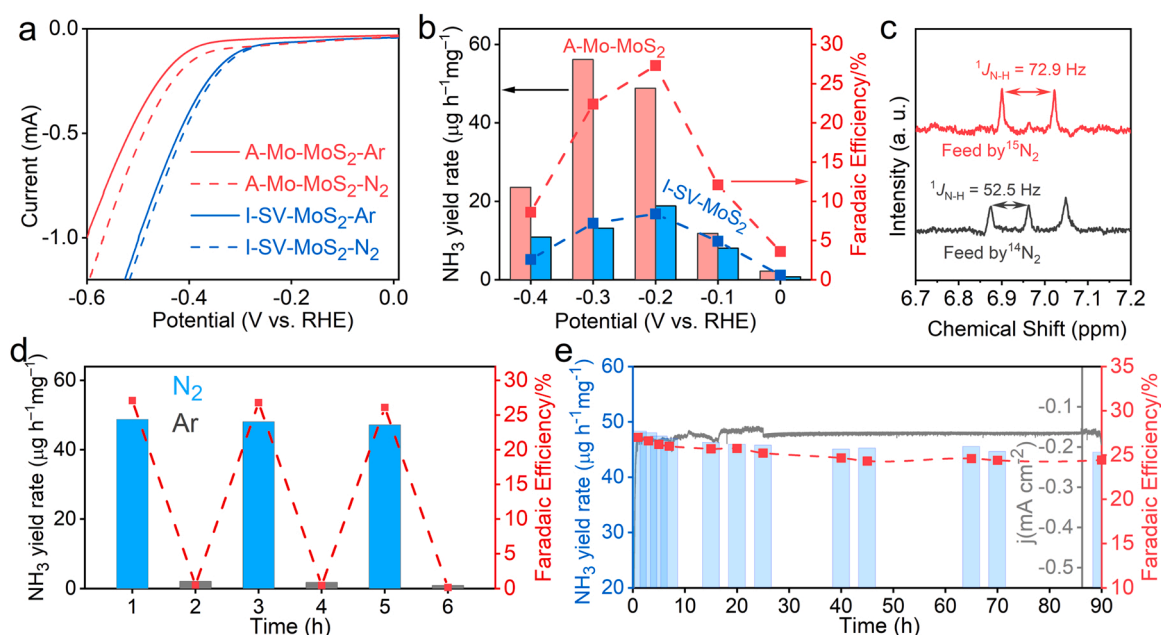


Fig. 2. (a) LSV curves of A-Mo-MoS₂ and I-SV-MoS₂ in Ar-saturated and N₂-saturated 0.1 M KCl solution with a scan rate of 5 mV s⁻¹. (b) NH₃ yield rate and Faradaic efficiency of A-Mo-MoS₂ and I-SV-MoS₂. (c) Isotopic labeling results with using ¹⁴N₂ or ¹⁵N₂ as the nitrogen source, respectively. (d) The change of NH₃ yield rate of A-Mo-MoS₂ under N₂ and Ar pumping per hour. (e) Stability test of A-Mo-MoS₂.

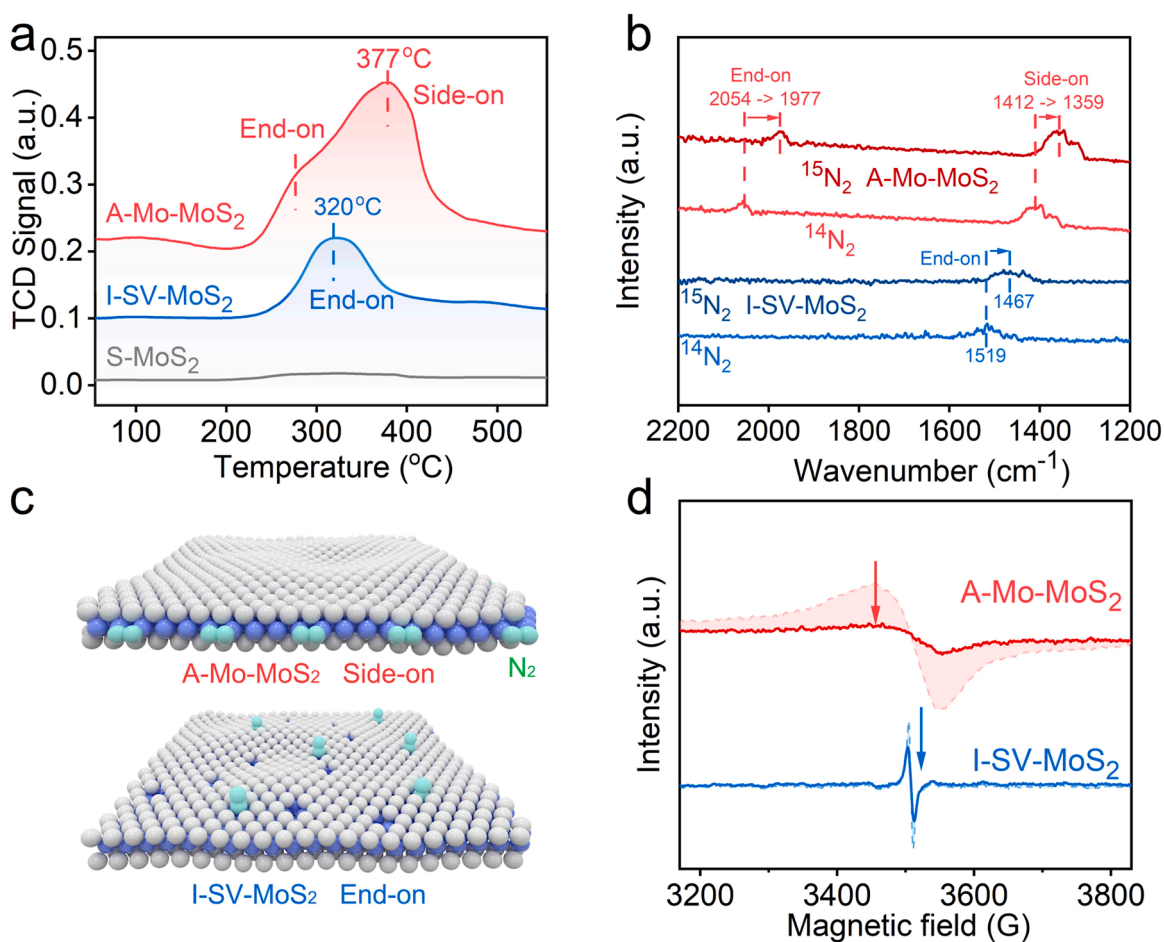


Fig. 3. (a) N₂-TPD spectra of A-Mo-MoS₂ and I-SV-MoS₂. (b) FTIR spectra of A-Mo-MoS₂ and I-SV-MoS₂. (c). (d) ESR spectra of A-Mo-MoS₂ and I-SV-MoS₂ after N₂ saturated absorption.

for all the samples, confirming their high selectivity toward NH_3 (Figs. S15–17). Furthermore, we found the apparent activation energy (E_a) of A-Mo-MoS₂ was 5.9 kJ mol⁻¹, significantly lower than that of I-SV-MoS₂ (20.3 kJ mol⁻¹) for N_2 fixation, by calculating the NH_3 yield rate at -0.20 V vs. RHE under different temperatures (Figs. S18, S19). The smaller E_a of A-Mo-MoS₂ verified its faster kinetic process.

To identify the source of produced NH_3 , the isotope labeling experiment with ¹⁵N-labeled N_2 as the reagent was utilized to confirm the origin of NH_3 (Figs. S20–22) [66]. Three characteristic peaks with a spacing of 52.5 Hz appeared in ¹H NMR spectra when using ¹⁴N-labeled N_2 as the reagent; while only two prominent peaks with a spacing of 72.9 Hz were observed in ¹H NMR spectra with ¹⁵N-labeled N_2 as the electrolyte (Fig. 2c), confirming that the generated NH_3 emanated from N_2 reduction rather than contaminations [67]. Meanwhile, we performed the alternated N_2 -Ar cycling measurements, and interestingly found that NH_3 was detected just in the case of N_2 -bubbling (Figs. 2d and S23), suggesting that the detected NH_3 indeed came from N_2 . More importantly, the A-Mo-MoS₂ exhibited great robustness and durability during continuous 90 h long-term electrochemical N_2 fixation or 12 consecutive cycles at -0.20 V vs. RHE, with almost no decrease of NH_3 yield rate and FE (Figs. 2e and S24–26). By contrast, only 60 % of both NH_3 yield rate and FE were retained for I-SV-MoS₂ after just 45 h or 5 cycles of reaction (Figs. S27 and S28).

We thus carried out the N_2 affinity tests using the temperature-programmed desorption of N_2 (N_2 -TPD) to deeply understand the different N_2 fixation activity of A-Mo-MoS₂, I-SV-MoS₂, and S-MoS₂ (Fig. 3a). A prominent desorption peak at 377 °C appeared in the N_2 -TPD curve of A-Mo-MoS₂, corresponding to the side-on adsorption of N_2 . Also, we observed a weak shoulder-like peak for A-Mo-MoS₂, assigned to

the end-on adsorption of N_2 . Obviously, the adjacent Mo sites might be more favorable for the side-on adsorption of N_2 . Differently, only end-on manner of N_2 adsorption occurred in the case of I-SV-MoS₂ with just a strong desorption peak at 320 °C. Expectedly, no N_2 desorption peak of S-MoS₂ confirmed that the Mo atoms or SVs were indispensable for the N_2 adsorption, which was further supported by the in situ diffuse reflectance Fourier transform infrared (FTIR) spectroscopy measurements (Fig. 3b, c). Similarly, two vibration peaks appeared on A-Mo-MoS₂, corresponding to end-on and side-on configurations with the side-on mode dominated. When ¹⁵N₂ was fed, the two peaks were red-shifted to low wavenumber on account of the isotopic effect. Also, I-SV-MoS₂ merely possessed an exclusive end-on N_2 adsorption configuration, in agreement with the N_2 -TPD measurements. Considering that the lower wavenumber of the N_2 adsorption peak corresponds to the weaker $\text{N}\equiv\text{N}$ triple bond [68], the A-Mo-MoS₂ obviously had a stronger ability to significantly weaken the $\text{N}\equiv\text{N}$ triple bond. To unravel the effect of unpaired spin-polarized electrons around active sites, we thermally treated the A-Mo-MoS₂ and I-SV-MoS₂ in N_2 atmosphere to reach N_2 adsorption saturated state, and interestingly found that the intensity of spin-delocalized electrons in A-Mo-MoS₂ more remarkably decreased than that of spin-localized electrons in I-SV-MoS₂ (Fig. 3d), suggesting that more spin-delocalized electrons would populate into the π -anti-bonding orbital of N_2 to facilitate the cleavage of robust $\text{N}\equiv\text{N}$.

3.3. DFT calculations

We then employed the density functional theory (DFT) calculations to understand the contributions of spin-delocalized and spin-localized electrons to the N_2 activation. The atomic models of A-Mo-MoS₂ and I-

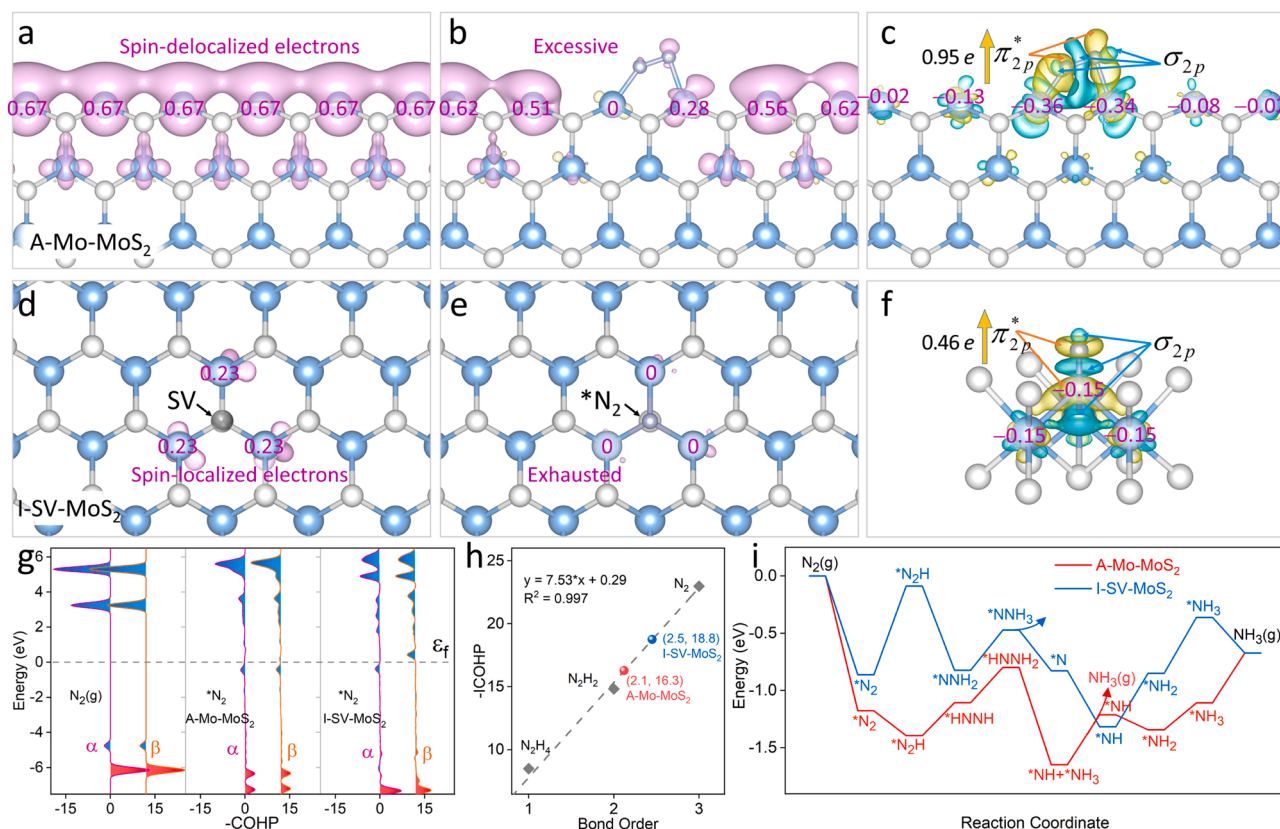


Fig. 4. The distribution of spin-delocalized electrons of A-Mo-MoS₂ (a) before and (b) after N_2 adsorption. (c) Charge density difference of N_2 adsorbed on A-Mo-MoS₂. The distribution of spin-localized electrons of I-SV-MoS₂ (d) before and (e) after N_2 adsorption. (f) Charge density difference of N_2 adsorbed on I-SV-MoS₂. The yellow and blue iso-surfaces with an iso-value of 0.005 au represent spatial charge accumulation and depletion, respectively. (g) The COHP analysis of gas phases and adsorbed N_2 . (h) The estimated bond order of *N_2 on A-Mo-MoS₂ and I-SV-MoS₂ via COHP analysis. (i) The Gibbs free energy changes of electrocatalytic N_2 fixation process as a function of the reaction coordinate at A-Mo-MoS₂ and I-SV-MoS₂. Color code: Mo in dusty blue, S in white, N in grey and SV in dark grey, respectively.

SV-MoS₂ were respectively established according to the experimental HAADF-STEM images. For A-Mo-MoS₂, the outermost individual Mo atom possessed ~ 0.67 spin-polarized electrons due to its highly unsaturated coordination. Interestingly, these spin-polarized electrons were overlapped and delocalized along the Mo edge, thus forming a spin-delocalized electrons field (Figs. 4a and S29). To visualize the function of these spin-delocalized electrons in N₂ activation, we introduced a N₂ molecule to be adsorbed on A-Mo-MoS₂ spontaneously. We found that N₂ molecule preferred to be captured by two adjacent Mo atoms via a side-on configuration with an adsorption energy of -1.18 eV, much stronger than an end-on adsorption configuration (-0.71 eV), which was in accordance with the above FTIR and N₂-TPD results. We further sought to compare the change of spin-delocalized electrons on A-Mo-MoS₂ before and after N₂ activation quantitatively. During the N₂ activation, the two directly bonding Mo atoms transferred approximately $1.06e$ to the π -antibonding orbital of adsorbed N₂ (*N_2). Also, the Mo atoms far away from the adsorbed sites donated their $0.37e$ spin-polarized electrons across the adjacent Mo atomic channel to take part in N₂ activation because of their delocalization nature (Fig. 4b). We interestingly found that there were still some residual electrons on adjacent Mo sites after the N₂ adsorption, suggesting that these spin-delocalized electrons on A-Mo-MoS₂ were excessive for the efficient N₂ activation. Further studies showed that the net electron increase of *N_2 was up to $0.95e$, respectively originating from the directly bonding Mo atoms ($0.70e$) and non-bonding Mo atoms ($0.25e$), as evidenced by the charge density difference and Bader charge analysis (Fig. 4c). In a sharp contrast to A-Mo-MoS₂, the individual Mo atom around SV of I-SV-MoS₂ was just charged with ~ 0.23 spin-polarized electrons, much less than that of adjacent Mo atom on A-Mo-MoS₂. Meanwhile, these spin-polarized electrons were obviously localized to individual SV with insignificant electron's donation from other distant SVs, so that these limited spin-localized electrons were nearly exhausted after the N₂ adsorption (Fig. 4d, e). These limitations led to the net electron increase of *N_2 to be merely $0.46e$ and thus the insufficient activation of N₂ (Fig. 4f), inferior to A-Mo-MoS₂ with spin-delocalized electrons.

We further compared the activation degree of *N_2 on A-Mo-MoS₂ and I-SV-MoS₂ by performing the crystal orbital Hamilton population (COHP), because the negative values of integrated COHP (ICOHP) by calculating the energy integral up to the Fermi level is an indicator of N≡N bond strength quantitatively [42–45]. After N₂ adsorbed on A-Mo-MoS₂, the Mo's spin-delocalized electrons injected into the anti-bonding orbital of *N_2 were located below the Fermi level of *N_2 with spin-up (α) and spin-down (β) states (Fig. 4g), resulting in the ICOHP of *N_2 reduced from 23.0 eV to 16.3 eV, implying that N≡N triple bond was largely weakened. By fitting the ICOHP as a function of N–N bond order with N₂, N₂H₂, and N₂H₄ as references (Fig. S30 and Table S3), the bond order of *N_2 on A-Mo-MoS₂ was estimated to be 2.1 , together with the bond length of *N_2 enlarged from 1.11 Å to 1.24 Å, strongly confirming the sufficient activation of *N_2 (Figs. 4h, S31 and Table S4). However, only new spin-up (α) state was found below the Fermi level for *N_2 on I-SV-MoS₂, along with the ICOHP of *N_2 decreased from 23.0 eV to 18.8 eV and the bond order reduced from 3.0 to 2.5 with the bond length of 1.20 Å. These theoretical results strongly demonstrated that the *N_2 could be more effectively activated by spin-delocalized electrons on A-Mo-MoS₂ than spin-localized electrons on I-SV-MoS₂.

To better understand the activity differences between A-Mo-MoS₂ and I-SV-MoS₂, we further calculated the Gibbs free energy of all possible elementary steps (Figs. 4i, S32–35 and Table S5). Similar with most reported catalysts, the rate-determining step (RDS) of I-SV-MoS₂ was the first protonation step of *N_2 to *NNH with a formidable barrier energy of 0.77 eV [69]. Nevertheless, this tough step became a spontaneous process on A-Mo-MoS₂, and its RDS was switched to the hydrogenation of *HNNH intermediate to *HNNH_2 with a surmountable barrier energy (0.31 eV). This RDS transition may be arisen from the sufficient spin-delocalized electrons on adjacent Mo sites, which enabled

the transformation of *N_2 to *NNH quickly. We further noted that the *HNNH_2 species was prone to form the $^*NH + ^*NH_3$ with a spontaneous N–N bond dissociation process, rather than the formation of *H_2NNH_2 , a potential intermediate to produce undesirable N₂H₄, explaining the high selectivity towards NH₃ of A-Mo-MoS₂.

Regarding that the parasitic hydrogen evolution reaction (HER) dramatically competes with N₂ reduction [70], we further sought to elucidate the origin of the enhanced catalytic selectivity toward NH₃ for A-Mo-MoS₂. We first compared the binding energies of N₂ and H₂O on A-Mo-MoS₂ and found that the binding energies of N₂ (-1.18 eV) was much stronger than that of H₂O (-0.46 eV) (Fig. S36 and Table S6), indicating that A-Mo-MoS₂ displayed a higher tendency toward N₂ adsorption in aqueous solution. Furthermore, the Gibbs free energy of H⁺ intermediate was calculated to simulate the energy barrier of HER. As expected, the Gibbs free energy of H⁺ was up to 0.87 eV on A-Mo-MoS₂, suggesting that the formation of H₂ byproduct was greatly suppressed (Fig. S37) [71,72], which accordingly improved the electrocatalytic N₂ fixation efficiency.

4. Conclusions

In summary, we have for the first time developed a simple and mild approach to fabricate adjacent Mo sites on the outermost edge of single-layer MoS₂, aiming to create spin-delocalized electrons around catalytically active Mo sites, which was theoretically more favorable to activating robust N₂ effectively, compared to spin-localized electrons on traditionally I-SV-MoS₂. Impressively, the A-Mo-MoS₂ exhibited an exceptional N₂ fixation activity, three times that of I-SV-MoS₂. Theoretical calculation results suggested that this improved activity of A-Mo-MoS₂ was ascribable to the enormous spin-delocalized electrons field on adjacent Mo sites, significantly impairing the stubborn N≡N and simultaneously transiting the rate-determining step from the energy-demanding *N_2 hydrogenation to the surmountable *HNNH hydrogenation, consequently rendering the *N_2 activation easily. We believe that the manipulation of spin-delocalized electrons effect is a new strategy to promote N₂ activation, which can also guide the electrochemical activation and transformation of other small molecules (i.e., O₂, CH₄, CO₂) to chemicals.

CRedit authorship contribution statement

Guangming Zhan: Investigation, Data curation, Conceptualization, Methodology, Software, Writing – original draft. **Fengjiao Quan:** Data curation, Formal analysis. **Yancai Yao:** Funding acquisition, Investigation, Writing – review & editing. **Shengxi Zhao:** Methodology. **Xiufan Liu:** Software. **Huayu Gu:** Software. **Yi Huang:** Funding acquisition. **Xiao Liu:** Supervision. **Falong Jia:** Methodology. **Lizhi Zhang:** Project administration, Supervision, Writing – review & editing.

Declaration of Competing Interest

The authors declare that they have no known competing financial interests or personal relationships that could have appeared to influence the work reported in this paper.

Data Availability

Data will be made available on request.

Acknowledgements

This work was supported by the National Natural Science Foundation of China (U21A20286 and 22102100), the National Key Research and Development Program of China (2021YFA1201701), Key Program of Shenzhen Science and Technology Commission (JCYJ20220818095601002), and the Natural Science Foundation of

Shanghai (22ZR1431700). We thank the photoemission end station BL1W1B in the Beijing Synchrotron Radiation Facility (BSRF) for help with characterizations. The computations in this paper were run on the π 2.0 cluster supported by the Center for High Performance Computing at Shanghai Jiao Tong University.

Appendix A. Supporting information

Supplementary data associated with this article can be found in the online version at [doi:10.1016/j.apcatb.2022.122186](https://doi.org/10.1016/j.apcatb.2022.122186).

References

- [1] B.H.R. Suryanto, K. Matuszek, J. Choi, R.Y. Hodgetts, H.-L. Du, J.M. Bakker, C.S. M. Kang, P.V. Cherepanov, A.N. Simonov, D.R. MacFarlane, Nitrogen reduction to ammonia at high efficiency and rates based on a phosphonium proton shuttle, *Science* 372 (2021) 1187–1191.
- [2] H.-L. Du, M. Chatti, R.Y. Hodgetts, P.V. Cherepanov, C.K. Nguyen, K. Matuszek, D. R. MacFarlane, A.N. Simonov, Electroreduction of nitrogen with almost 100 % current-to-ammonia efficiency, *Nature* 609 (2022) 722–727.
- [3] L. Jie, L. Qian, A. Abdulmohsen Ali, S. Xuping, Recent advances in nanostructured heterogeneous catalysts for N-cycle electrocatalysis, *Nano Res.* 1 (2022), e9120010.
- [4] A.R. Singh, B.A. Rohr, J.A. Schwalbe, M. Carnello, K. Chan, T.F. Jaramillo, I. Chorkendorff, J.K. Nørskov, Electrochemical ammonia synthesis—the selectivity challenge, *ACS Catal.* 7 (2016) 706–709.
- [5] J.H. Montoya, C. Tsai, A. Vojvodic, J.K. Nørskov, The challenge of electrochemical ammonia synthesis: a new perspective on the role of nitrogen scaling relations, *ChemSusChem* 8 (2015) 2180–2186.
- [6] Q. Liu, Y. Lin, S. Gu, Z. Cheng, L. Xie, S. Sun, L. Zhang, Y. Luo, A.A. Alshehri, M. S. Hamdy, Q. Kong, J. Wang, X. Sun, Enhanced N_2 -to- NH_3 conversion efficiency on Cu_3P nanoribbon electrocatalyst, *Nano Res.* 15 (2022) 7134–7138.
- [7] H.P. Jia, E.A. Quadrelli, Mechanistic aspects of dinitrogen cleavage and hydrogenation to produce ammonia in catalysis and organometallic chemistry: relevance of metal hydride bonds and dihydrogen, *Chem. Soc. Rev.* 43 (2014) 547–564.
- [8] T. Kandemir, M.E. Schuster, A. Senyshyn, M. Behrens, R. Schlögl, The Haber–Bosch process revisited: on the real structure and stability of “ammonia iron” under working conditions, *Angew. Chem. Int. Ed.* 52 (2013) 12723–12726.
- [9] J. Wang, B. Huang, Y. Ji, M. Sun, T. Wu, R. Yin, X. Zhu, Y. Li, Q. Shao, X. Huang, A general strategy to glassy M-Te (M = Ru, Rh, Ir) porous nanorods for efficient electrochemical N_2 fixation, *Adv. Mater.* 32 (2020) 1907112.
- [10] C. Yang, B. Huang, S. Bai, Y. Feng, Q. Shao, X. Huang, A generalized surface chalcogenation strategy for boosting the electrochemical N_2 fixation of metal nanocrystals, *Adv. Mater.* 32 (2020) 2001267.
- [11] C. Liu, S. Li, Z. Li, L. Zhang, H. Chen, D. Zhao, S. Sun, Y. Luo, A.A. Alshehri, M. S. Hamdy, Q. Liu, X. Sun, Ambient N_2 -to- NH_3 fixation over a CeO_2 nanoparticle decorated three-dimensional carbon skeleton, *Sustainable, Energy Fuels* 6 (2022) 3344–3348.
- [12] H.-j. Chen, Z.-q. Xu, S. Sun, Y. Luo, Q. Liu, M.S. Hamdy, Z.-s. Feng, X. Sun, Y. Wang, Plasma-etched Ti_2O_3 with oxygen vacancies for enhanced NH_3 electrosynthesis and Zn–Ni batteries, *Inorg. Chem. Front.* 9 (2022) 4608–4613.
- [13] X. Cui, C. Tang, Q. Zhang, A review of electrocatalytic reduction of dinitrogen to ammonia under ambient conditions, *Adv. Energy Mater.* 8 (2018) 1800369.
- [14] G. Lin, Q. Ju, X. Guo, W. Zhao, S. Adimi, J. Ye, Q. Bi, J. Wang, M. Yang, F. Huang, Intrinsic electron localization of metastable MoS_2 boosts electrocatalytic nitrogen reduction to ammonia, *Adv. Mater.* 33 (2021) 2007509.
- [15] L. Zhang, X. Ji, X. Ren, Y. Ma, X. Shi, Z. Tian, A.M. Asiri, L. Chen, B. Tang, X. Sun, Electrochemical ammonia synthesis via nitrogen reduction reaction on a MoS_2 catalyst: theoretical and experimental studies, *Adv. Mater.* 30 (2018), e1800191.
- [16] Y. Liu, M. Han, Q. Xiong, S. Zhang, C. Zhao, W. Gong, G. Wang, H. Zhang, H. Zhao, Dramatically enhanced ambient ammonia electrosynthesis performance by in-operando created Li-S interactions on MoS_2 electrocatalyst, *Adv. Energy Mater.* 9 (2019) 1803935.
- [17] X. Li, T. Li, Y. Ma, Q. Wei, Y. Qiu, H. Guo, X. Shi, P. Zhang, A.M. Asiri, L. Chen, B. Tang, X. Sun, Boosted electrocatalytic N_2 reduction to NH_3 by defect-rich MoS_2 nanoflower, *Adv. Energy Mater.* 8 (2018) 1801357.
- [18] J. Zhao, Z. Chen, Single Mo atom supported on defective boron nitride monolayer as an efficient electrocatalyst for nitrogen fixation: a computational study, *J. Am. Chem. Soc.* 139 (2017) 12480–12487.
- [19] M.-A. L  gar  , G. B  langer-Chabot, R.D. Dewhurst, E. Welz, I. Krummenacher, B. Engels, H. Braunschweig, Nitrogen fixation and reduction at boron, *Science* 359 (2018) 896–900.
- [20] C. Tang, S.-Z. Qiao, How to explore ambient electrocatalytic nitrogen reduction reliably and insightfully, *Chem. Soc. Rev.* 48 (2019) 3166–3180.
- [21] F. Lai, J. Huang, X. Liao, W. Zong, L. Ge, F. Gan, Y. Fang, Y.-E. Miao, J. Hofkens, T. Liu, L. Dai, Semicrystalline conjugated polymers with well-defined active sites for nitrogen fixation in a seawater electrolyte, *Adv. Mater.* 34 (2022) 2201853.
- [22] S.Z. Andersen, V.   li  , S. Yang, J.A. Schwalbe, A.C. Nielander, J.M. McEnaney, K. Enemark-Rasmussen, J.G. Baker, A.R. Singh, B.A. Rohr, M.J. Statt, S.J. Blair, S. Mezavilla, J. Kibsgaard, P.C.K. Vesborg, M. Carnello, S.F. Bent, T.F. Jaramillo, I.E.L. Stephens, J.K. N  rskov, I. Chorkendorff, A rigorous electrochemical ammonia synthesis protocol with quantitative isotope measurements, *Nature* 570 (2019) 504–508.
- [23] J. Zhang, X. Tian, M. Liu, H. Guo, J. Zhou, Q. Fang, Z. Liu, Q. Wu, J. Lou, Cobalt-modulated molybdenum–dinitrogen interaction in MoS_2 for catalyzing ammonia synthesis, *J. Am. Chem. Soc.* 141 (2019) 19269–19275.
- [24] S. Chen, X. Liu, J. Xiong, L. Mi, Y. Li, Engineering strategies for boosting the nitrogen reduction reaction performance of MoS_2 -based electrocatalysts, *Mater. Today Nano* 18 (2022), 100202.
- [25] X.-F. Li, Q.-K. Li, J. Cheng, L. Liu, Q. Yan, Y. Wu, X.-H. Zhang, Z.-Y. Wang, Q. Qiu, Y. Luo, Conversion of dinitrogen to ammonia by FeN_3 -embedded graphene, *J. Am. Chem. Soc.* 138 (2016) 8706–8709.
- [26] J.G. Roch, G. Froehlicher, N. Leisgang, P. Makk, K. Watanabe, T. Taniguchi, R. J. Warburton, Spin-polarized electrons in monolayer MoS_2 , *Nat. Nanotechnol.* 14 (2019) 432–436.
- [27] J. Hu, L. Yu, J. Deng, Y. Wang, K. Cheng, C. Ma, Q. Zhang, W. Wen, S. Yu, Y. Pan, J. Yang, H. Ma, F. Qi, Y. Wang, Y. Zheng, M. Chen, R. Huang, S. Zhang, Z. Zhao, J. Mao, X. Meng, Q. Ji, G. Hou, X. Han, X. Bao, Y. Wang, D. Deng, Sulfur vacancy-rich MoS_2 as a catalyst for the hydrogenation of CO_2 to methanol, *Nat. Catal.* 4 (2021) 242–250.
- [28] Y. Sun, S. Ding, B. Xia, J. Duan, M. Antonietti, S. Chen, Biomimetic $FeMo(Se, Te)$ as joint electron pool promoting nitrogen electrofixation, *Angew. Chem. Int. Ed.* 61 (2022), e202115198.
- [29] M.V. Bollinger, J.V. Lauritsen, K.W. Jacobsen, J.K. N  rskov, S. Helveg, F. Besenbacher, One-dimensional metallic edge states in MoS_2 , *Phys. Rev. Lett.* 87 (2001), 196803.
- [30] J.V. Lauritsen, J. Kibsgaard, S. Helveg, H. Topsoe, B.S. Clausen, E. Laegsgaard, F. Besenbacher, Size-dependent structure of MoS_2 nanocrystals, *Nat. Nanotechnol.* 2 (2007) 53–58.
- [31] R.V. Mom, J.N. Louwen, J.W.M. Frenken, I.M.N. Groot, In situ observations of an active MoS_2 model hydrodesulfurization catalyst, *Nat. Commun.* 10 (2019) 2546.
- [32] S.S. Gronborg, N. Salazar, A. Bruix, J. Rodriguez-Fernandez, S.D. Thomsen, B. Hammer, J.V. Lauritsen, Visualizing hydrogen-induced reshaping and edge activation in MoS_2 and Co-promoted MoS_2 catalyst clusters, *Nat. Commun.* 9 (2018) 2211.
- [33] L. Zhang, J. Liang, Y. Wang, T. Mou, Y. Lin, L. Yue, T. Li, Q. Liu, Y. Luo, N. Li, B. Tang, Y. Liu, S. Gao, A.A. Alshehri, X. Guo, D. Ma, X. Sun, High-performance electrochemical NO reduction into NH_3 by MoS_2 nanosheet, *Angew. Chem. Int. Ed.* 60 (2021) 25263–25268.
- [34] W. Kohn, L.J. Sham, Self-consistent equations including exchange and correlation effects, *Phys. Rev.* 140 (1965) A1133–A1138.
- [35] P. Hohenberg, W. Kohn, Inhomogeneous electron gas, *Phys. Rev.* 136 (1964) B864–B871.
- [36] G. Kresse, J. Furthm  ller, Efficient iterative schemes for ab initio total-energy calculations using a plane-wave basis set, *Phys. Rev. B* 54 (1996) 11169–11186.
- [37] J.P. Perdew, K. Burke, M. Ernzerhof, Generalized gradient approximation made simple, *Phys. Rev. Lett.* 77 (1996) 3865–3868.
- [38] G. Kresse, D. Joubert, From ultrasoft pseudopotentials to the projector augmented-wave method, *Phys. Rev. B* 59 (1999) 1758–1775.
- [39] P.E. Bl  chl, Projector augmented-wave method, *Phys. Rev. B* 50 (1994) 17953–17979.
- [40] S. Grimme, Semiempirical GGA-type density functional constructed with a long-range dispersion correction, *J. Comput. Chem.* 27 (2006) 1787–1799.
- [41] J.K. N  rskov, T. Bligaard, A. Logadottir, J.R. Kitchin, J.G. Chen, S. Pandalov, J. K. N  rskov, Trends in the exchange current for hydrogen evolution, *J. Electrochem. Soc.* 152 (2005) J23–J26.
- [42] V.L. Deringer, A.L. Tchougreff, R. Dronskowski, Crystal orbital Hamilton population (COHP) analysis as projected from plane-wave basis sets, *J. Phys. Chem. A* 115 (2011) 5461–5466.
- [43] R. Dronskowski, P.E. Blochl, Crystal orbital Hamilton populations (COHP) - energy-resolved visualization of chemical bonding in solids based on density-functional calculations, *J. Phys. Chem.* 97 (1993) 8617–8624.
- [44] S. Maintz, V.L. Deringer, A.L. Tchougreff, R. Dronskowski, Analytic projection from plane-wave and PAW wavefunctions and application to chemical-bonding analysis in solids, *J. Comput. Chem.* 34 (2013) 2557–2567.
- [45] S. Maintz, V.L. Deringer, A.L. Tchougreff, R. Dronskowski, LOBSTER: a tool to extract chemical bonding from plane-wave based DFT, *J. Comput. Chem.* 37 (2016) 1030–1035.
- [46] J. Li, S. Chen, F. Quan, G. Zhan, F. Jia, Z. Ai, L. Zhang, Accelerated dinitrogen electroreduction to ammonia via interfacial polarization triggered by single-atom protrusions, *Chem* 6 (2020) 885–901.
- [47] J.N. Coleman, M. Lotya, A. O’Neill, S.D. Bergin, P.J. King, U. Khan, K. Young, A. Gaucher, S. De, R.J. Smith, I.V. Shvets, S.K. Arora, G. Stanton, H.-Y. Kim, K. Lee, G.T. Kim, G.S. Duesberg, T. Hallam, J.J. Boland, J.J. Wang, J.F. Donegan, J. C. Grunlan, G. Moriarty, A. Shmeliov, R.J. Nicholls, J.M. Perkins, E.M. Grieveson, K. Theuwissen, D.W. McComb, P.D. Nellist, V. Nicolosi, Two-dimensional nanosheets produced by liquid exfoliation of layered materials, *Science* 331 (2011) 568–571.
- [48] Y.-H. Lee, X.-Q. Zhang, W. Zhang, M.-T. Chang, C.-T. Lin, K.-D. Chang, Y.-C. Yu, J. T.-W. Wang, C.-S. Chang, L.-J. Li, T.-W. Lin, Synthesis of large-area MoS_2 atomic layers with chemical vapor deposition, *Adv. Mater.* 24 (2012) 2320–2325.
- [49] J. Polz, H. Zeilinger, B. M  ller, H. Kn  zinger, Hydrogen uptake by MoS_2 and sulfided alumina-supported Mo catalysts, *J. Catal.* 120 (1989) 22–28.
- [50] L. Li, Z. Qin, L. Ries, S. Hong, T. Michel, J. Yang, C. Salameh, M. Bechelany, P. Miele, D. Kaplan, M. Chhowalla, D. Voiry, Role of sulfur vacancies and undercoordinated Mo regions in MoS_2 nanosheets toward the evolution of hydrogen, *ACS Nano* 13 (2019) 6824–6834.

- [51] R. Stoyanova, M. Gorova, E. Zhecheva, EPR of Mn^{4+} in spinels $Li_{1+x}Mn_{2-x}O_4$ with $0 \leq x \leq 0.1$, *J. Phys. Chem. Sol.* 61 (2000) 609–614.
- [52] A.I. Shames, E.A. Katz, A.M. Panich, D. Mogilyansky, E. Mogilko, J. Grinblat, V. P. Belousov, I.M. Belousova, A.N. Ponomarev, Structural and magnetic resonance study of astralen nanoparticles, *Diam. Relat. Mater.* 18 (2009) 505–510.
- [53] C.P. Poole, *Electron Spin Resonance: A Comprehensive Treatise on Experimental Techniques*, John Wiley, New York, 1996.
- [54] B.H.R. Suryanto, H.-L. Du, D. Wang, J. Chen, A.N. Simonov, D.R. MacFarlane, Challenges and prospects in the catalysis of electroreduction of nitrogen to ammonia, *Nat. Catal.* 2 (2019) 290–296.
- [55] X. Ren, J. Zhao, Q. Wei, Y. Ma, H. Guo, Q. Liu, Y. Wang, G. Cui, A.M. Asiri, B. Li, B. Tang, X. Sun, High-performance N_2 -to- NH_3 conversion electrocatalyzed by Mo_2C nanorod, *ACS Cent. Sci.* 5 (2019) 116–121.
- [56] L. Zhang, X. Ji, X. Ren, Y. Luo, X. Shi, A.M. Asiri, B. Zheng, X. Sun, Efficient electrochemical N_2 reduction to NH_3 on MoN nanosheets array under ambient conditions, *ACS Sustain. Chem. Eng.* 6 (2018) 9550–9554.
- [57] H. Cheng, L.X. Ding, G.F. Chen, L. Zhang, J. Xue, H. Wang, Molybdenum carbide nanodots enable efficient electrocatalytic nitrogen fixation under ambient conditions, *Adv. Mater.* 30 (2018), e1803694.
- [58] L. Han, X. Liu, J. Chen, R. Lin, H. Liu, F. Lu, S. Bak, Z. Liang, S. Zhao, E. Stavitski, J. Luo, R.R. Adzic, H.L. Xin, Atomically dispersed molybdenum catalysts for efficient ambient nitrogen fixation, *Angew. Chem. Int. Ed.* 58 (2019) 2321–2325.
- [59] X. Ren, G. Cui, L. Chen, F. Xie, Q. Wei, Z. Tian, X. Sun, Electrochemical N_2 fixation to NH_3 under ambient conditions: Mo_2N nanorod as a highly efficient and selective catalyst, *Chem. Commun.* 54 (2018) 8474–8477.
- [60] L. Zeng, S. Chen, J. van der Zalm, X. Li, A. Chen, Sulfur vacancy-rich N-doped MoS_2 nanoflowers for highly boosting electrocatalytic N_2 fixation to NH_3 under ambient conditions, *Chem. Commun.* 55 (2019) 7386–7389.
- [61] J. Han, X. Ji, X. Ren, G. Cui, L. Li, F. Xie, H. Wang, B. Li, X. Sun, MoO_3 nanosheets for efficient electrocatalytic N_2 fixation to NH_3 , *J. Mater. Chem. A* 6 (2018) 12974–12977.
- [62] X. Li, X. Ren, X. Liu, J. Zhao, X. Sun, Y. Zhang, X. Kuang, T. Yan, Q. Wei, D. Wu, A. MoS_2 nanosheet–reduced graphene oxide hybrid: an efficient electrocatalyst for electrocatalytic N_2 reduction to NH_3 under ambient conditions, *J. Mater. Chem. A* 7 (2019) 2524–2528.
- [63] D. Yang, T. Chen, Z. Wang, Electrochemical reduction of aqueous nitrogen (N_2) at a low overpotential on (110)-oriented Mo nanofilm, *J. Mater. Chem. A* 5 (2017) 18967–18971.
- [64] G. Zhang, Q. Ji, K. Zhang, Y. Chen, Z. Li, H. Liu, J. Li, J. Qu, Triggering surface oxygen vacancies on atomic layered molybdenum dioxide for a low energy consumption path toward nitrogen fixation, *Nano Energy* 59 (2019) 10–16.
- [65] B.H.R. Suryanto, D. Wang, L.M. Azofra, M. Harb, L. Cavallo, R. Jalili, D.R. G. Mitchell, M. Chatti, D.R. MacFarlane, MoS_2 polymorphic engineering enhances selectivity in the electrochemical reduction of nitrogen to ammonia, *ACS Energy Lett.* 4 (2018) 430–435.
- [66] M. Wang, S. Liu, T. Qian, J. Liu, J. Zhou, H. Ji, J. Xiong, J. Zhong, C. Yan, Over 56.55 % Faradaic efficiency of ambient ammonia synthesis enabled by positively shifting the reaction potential, *Nat. Commun.* 10 (2019) 341.
- [67] J. Liu, M.S. Kelley, W. Wu, A. Banerjee, A.P. Douvalis, J. Wu, Y. Zhang, G.C. Schatz, M.G. Kanatzidis, Nitrogenase-mimic iron-containing chalcogels for photochemical reduction of dinitrogen to ammonia, *Proc. Natl. Acad. Sci. USA* 113 (2016) 5530–5535.
- [68] C. Mao, J. Wang, Y. Zou, H. Li, G. Zhan, J. Li, J. Zhao, L. Zhang, Anion (O, N, C, and S) vacancies promoted photocatalytic nitrogen fixation, *Green Chem.* 21 (2019) 2852–2867.
- [69] S. Liu, M. Wang, T. Qian, H. Ji, J. Liu, C. Yan, Facilitating nitrogen accessibility to boron-rich covalent organic frameworks via electrochemical excitation for efficient nitrogen fixation, *Nat. Commun.* 10 (2019) 3898.
- [70] C. Choi, G.H. Gu, J. Noh, H.S. Park, Y. Jung, Understanding potential-dependent competition between electrocatalytic dinitrogen and proton reduction reactions, *Nat. Commun.* 12 (2021) 4353.
- [71] J. Dai, Y. Zhu, Y. Chen, X. Wen, M. Long, X. Wu, Z. Hu, D. Guan, X. Wang, C. Zhou, Q. Lin, Y. Sun, S.-C. Weng, H. Wang, W. Zhou, Z. Shao, Hydrogen spillover in complex oxide multifunctional sites improves acidic hydrogen evolution electrocatalysis, *Nat. Commun.* 13 (2022) 1189.
- [72] S. Huang, B. Gong, Y. Jin, P.H.L. Sit, J.C.-H. Lam, The structural phase effect of MoS_2 in controlling the reaction selectivity between electrocatalytic hydrogenation and dimerization of furfural, *ACS Catal.* 12 (2022) 11340–11354.